International Journal of Impact Engineering 171 (2023) 104369

Contents lists available at ScienceDirect

International Journal of Impact Engineering

journal homepage: www.elsevier.com/locate/ijimpeng

Reconstruction of surface pressures on flat plates impacted by blast waves using the Virtual Fields Method

Rene Kaufmann [a,b,*,1], Sindre Nordmark Olufsen [a,b,1], Egil Fagerholt [a,1], Vegard Aune [a,b,1]

[a] Structural Impact Laboratory (SIMLab), Department of Structural Engineering, Norwegian University of Science and Technology (NTNU), Trondheim, Norway
[b] Centre for Advanced Structural Analysis (CASA), NTNU, Trondheim, Norway

ARTICLE INFO

Keywords:
Pressure reconstruction
Virtual fields method
Thin steel plates
Blast–structure interaction

ABSTRACT

An accurate description of surface pressure loads imposed by blast waves is crucial for the design of the next generation of blast-resistant structures. However, experimental techniques for non-intrusive, full-field surface pressure measurements are not readily available. To address this challenge, a new application of the Virtual Fields Method (VFM) has been explored to reconstruct the surface pressures acting on thin steel plates using full-field deformation measurements of the plate dynamics. A shock tube facility was used to generate a blast-like loading in controlled, laboratory environments, where the plate dynamics were measured using the deflectometry technique. Different blockages at the shock tube exit allowed for varying the spatial distribution and temporal history of the blast loading. The surface pressures were reconstructed from experimentally measured kinematic fields using the VFM. A nearly non-deformable plate equipped with point-wise pressure sensors was also used to obtain a reference, allowing to assess the performance and reliability of the proposed methodology in capturing the surface pressure distributions. Moreover, visualizations of the different blast wave impacts on the plate were obtained using a background-oriented schlieren setup. Finally, the influence of potential error sources was investigated by means of a virtual laboratory using a finite element analysis to generate synthetic input to the load reconstruction analysis. The proposed methodology provided robust, precise predictions using noise-free input from virtual experiments. The presence of both systematic and random errors during the experimental campaign resulted in a reduced pressure reconstruction accuracy, where the peak pressure amplitudes were approximately 10–20% lower compared to the pointwise transducer data. Pressure reconstructions from experimental data still showed qualitatively good estimates of the pressure distributions that were extrapolated from transducer data. Hence, this work highlights the capabilities of a promising methodology to obtain more insight into the effective action of the loading during blast–structure interaction of plated structures.

1. Introduction

Civil engineering structures extend the scope of traditional safety and security design by also introducing architectural, lightweight and flexible structures. It is therefore of utmost importance to provide structural engineers with detailed knowledge of loads, underlying physics and materials to understand and predict how lightweight, flexible structures respond during blast loading events.

However, currently available blast loading measurement techniques offer limited capabilities for quantifying surface load distributions acting on an investigated structure.

Over the last decades, the advances in development of high-resolution, high-speed cameras have propelled the use of full-field, time-resolved deformation measurement techniques. Optical techniques such as digital image correlation (DIC), see Refs. [1–5], the grid method [6] and deflectometry [7] are now well-established and routinely used to detect and measure the motion and deformation of structures. However, the literature is rather scarce when it comes to experimental techniques providing robust, high-fidelity measurements of the space–time distribution of the surface pressures during blast–structure interaction. Current approaches are typically based on pointwise measurements on nearly non-deformable structures using pressure transducers, load cells or Hopkinson pressure bars [8–10]. There is a lack of measurement techniques to determine the full-field surface pressures which are necessary to investigate the two-way

* Corresponding author at: Structural Impact Laboratory (SIMLab), Department of Structural Engineering, Norwegian University of Science and Technology (NTNU), Trondheim, Norway.
E-mail address: rene.kaufmann@ntnu.no (R. Kaufmann).

[1] The authors declare that the present work is their own. They have created, acquired, and processed all presented data, text and figures.

https://doi.org/10.1016/j.ijimpeng.2022.104369
Received 8 February 2022; Received in revised form 6 August 2022; Accepted 25 August 2022
Available online 30 August 2022

interaction between the blast loading and the dynamic response of plated structures [11].

While there is a number of techniques available for surface pressure measurements, most are not suitable for full-field measurements or for the experimental conditions during blast events.

Pressure reconstruction within a fluid can be achieved using particle image velocimetry (PIV) and particle tracking velocimetry (PTV), which are established techniques for flow field measurements (see *e.g.* [12–14]). Velocity measurements within a fluid, *e.g.* using particle image velocimetry (PIV), particle tracking velocimetry (PTV) and optical flow tracking velocimetry (OFTV), can be used to reconstruct pressure from the obtained velocity fields (see *e.g.* [12–15]). These techniques require optical access to the flow field and traceable particles in the investigated fluid, which is usually not feasible in tests with blast loaded plates because of the limited optical access to the loaded side of the plate, as well as the risk to damage the optical equipment. Pressure sensitive paints (*e.g.* [16, chapter 4.4]) are often used for the measurement of large differential surface pressure amplitudes in shock tubes, but they also require optical access to the pressure side of the investigated structure.

A common and well established approach for measuring surface pressure is the integration of pressure transducers into the investigated surface. However, this technique yields pointwise measurements and a large number of pressure transducers is needed to capture spatial pressure distributions in detail. The spatial resolution that can be achieved this way is limited by the size of the transducers, as well as by the number of transducers that can be fitted into the tested structure. Mounting of the transducers requires holes to be drilled in the structure, which can further change the structural properties. A pointwise measurement approach for blast loading from buried explosives was developed in Refs. [8,9,17,18]. Here, the authors used arrays of Hopkinson pressure bars that allowed them to map the resulting blast load distributions.

Inverse analyses can also be used to obtain loading information based on deformation information of a structure subjected to blast loading. Dimensional analysis may be employed to relate the plate response to the loading conditions, but relies on assumptions on the symmetry of the problem, loading distributions and material properties [19–22]. Further, any empirically obtained equations are only valid in the experimental range in which they were obtained. Another approach is to reconstruct the surface pressure from full-field deformation measurements by solving the mechanical equilibrium equations governing the structural dynamics. It was employed in a series of studies where thin plates in pure bending were used as test samples (Refs. [23–31]). This allows using the Kirchhoff–Love theory for describing the equilibrium, relating transverse loading of the thin plate to the surface deformations. The corresponding equilibrium equation involves fourth order spatial and second order temporal derivatives of the surface deflections. These derivatives pose a key challenge for pressure reconstruction due to the amplification of experimental noise caused by numerical differentiation. Therefore, filtering approaches are crucial for extracting load information accurately from experimental data via the equilibrium equation. This is particularly challenging when investigating unknown transverse load distributions because the filters can bias signal amplitudes. One suitable technique for reducing the noise level was demonstrated in Refs. [23,24], where the authors employed wavenumber filters to regularize noisy deformation data from laser doppler vibrometer measurements. This allowed the authors to identify external mechanical vibration sources, as well as the acoustic component of a turbulent boundary layer on thin plates via the equilibrium equations. Further addressing experimental noise and noise amplification arising from numerical differentiation, the VFM was used in a number of studies. The VFM is an application of the principle of virtual work and allows using full-field data to identify constitutive mechanical material parameters from known loading or *vice versa* [32]. It further allows addressing the problem of thin plates in pure bending with the global equilibrium equation, reducing the order of spatial differentiations of the deflection field required for load reconstruction to two. Utilizing the virtual fields in the equilibrium equation as spatial filters offers an additional way to address spatial noise with this technique. Compared to finite element method analyses, the VFM is computationally cheap. Since the VFM is based on global equilibrium equations, a piecewise approach was developed to reconstruct spatial load distributions [33].

Several studies [25–27] used the VFM in combination with scanning laser-doppler vibrometer measurements to extract pressure distributions in the form of acoustic loads on plates and walls with a piecewise virtual fields approach. In order to acquire sufficient signal-to-noise ratios for the measured deflections that are required for load reconstruction, recent studies used deflectometry measurements. Deflectometry is an optical, highly sensitive technique that allows measuring changes in surface slopes [7]. While slopes require spatial integration to obtain the deflections for load reconstruction, they only require one spatial differentiation for load reconstruction with the principle of virtual work. This combination of deflectometry and the VFM allowed reconstructions of dynamic point loads from impact hammer and drop tests in Ref. [28] and of impinging air jets in Refs. [29–31]. A key challenge found in these studies on VFM pressure reconstruction was the accuracy of pressure amplitudes. The virtual fields act as low-pass filters and can introduce significant bias to the reconstructed pressure amplitude. Kaufmann et al. [29] addressed this issue by introducing an approach for the systematic assessment of accuracy and systematic processing error using simulated experiments.

The present study demonstrates an application of the VFM to reconstruct full-field surface pressures during the dynamic response of thin, blast loaded steel plates. This amends existing diagnostic techniques in blast environments towards full-field, non-intrusive measurement of surface pressure loads, as an alternative to point-wise measurements from pressure transducers and load cells. Compared to previous studies on blast loading, the new approach involving camera measurements poses challenges in terms of the experimental setup due to accessibility and vibrations, as well as due to the short relevant time scales of the events. A controlled, laboratory environment is used to generate three distinct blast wave fronts, further demonstrating the potential of the approach for identifying spatial loading and its distribution. The present study also uses pressure transducer array measurements on nearly non-deformable plates to establish a reference to evaluate the performance of the proposed methodology. In addition, background oriented schlieren (BOS) measurements are used to compare the reconstructed spatial distributions. Finally, virtual experiments based on a finite element analysis are carried out to evaluate the performance of the data processing and VFM pressure reconstruction methodology, eliminating experimental limitations and allowing an investigation of error sources.

2. Methodology

This section introduces the experimental setup, parameters, equipment, and optical techniques that were applied in this study, as well as a theoretical background of the pressure reconstruction approach. The final part describes the processing approach that is applied to the experimental data.

2.1. Setup for shock-tube experiments

Experiments were carried out in the SIMLab shock tube facility (SSTF) at the Department of Structural Engineering at NTNU. A detailed description of the shock tube facility is given in Ref. [34]. Fig. 1(a) shows a schematic of the facility and setup. The SSTF produces a planar shock wave in a controlled, laboratory environment. Different blockages at the end of the tube allowed generating different pressure

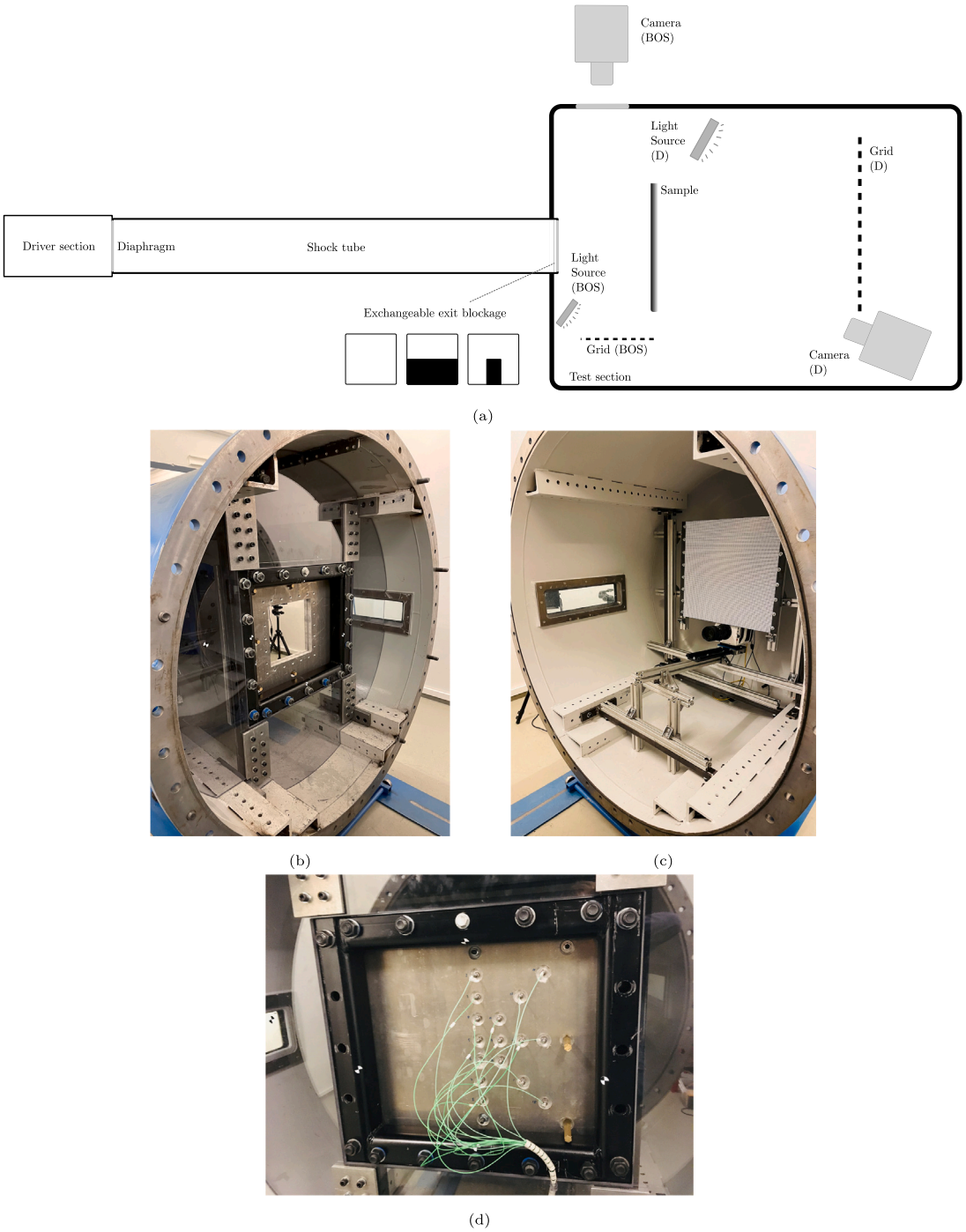

Fig. 1. Pictures of the setup components: (a) Schematic of the experimental setup in the shock tube facility with deflectometry (D) and background oriented schlieren (BOS) components, (b) Reflective test plate mounted on the rigid frame and perspex shield, (c) Camera and printed deflectometry grid and (d) Pressure transducer setup.

distributions on the test plate. In addition to the unblocked configuration, a half-blockage and a column shaped blockage were chosen (see Fig. 2). A steel plate with mirror-finish surface was used as test specimen, introducing a specular reflective surface which is necessary to use the deflectometry technique. The plate was placed 220 mm downstream from the blockages, with the reflective side facing away from the shock tube exit. The test plate was fixed between two 25 mm thick aluminum frames, *i.e.*, a mounting frame with outer dimensions 700 mm×800 mm and a clamping frame with outer dimension 400 mm × 400 mm. Both frames had a square opening at the center, leaving an exposed area of 300 mm × 300 mm for the test plate. Further downstream, a rigid frame was used to mount the camera and grid that are required for the deflectometry setup in the test section. A plastic wind shield was mounted around the steel frame holding the test plate to protect the optical setup, see Fig. 1(b). Two light sources were placed on either side and outside of the test section, illuminating the printed grid through windows in the sides of the test section. Due to the lack of large windows in the test section it was not possible to place the camera and grid outside of the test section. Additional tests using pressure transducers were carried out to validate the pressure reconstruction results. A 25 mm thick aluminum plate with outer dimensions 700 mm× 800 mm and pressure transducers fitted into the surface was placed in the same position as the polished steel test plate. 16 piezoelectric Kistler Type 603B pressure transducers recording at 500 kHz were used

Table 1
Setup parameters.

Optics		
Camera		Phantom v2511
Technology		CMOS
Camera pixel size		28 µm
Dynamic range		12 bit
Settings		
Resolution		512 × 512 pixels
Frame rate	f_{aq}	75 000 fps
Exposure		5 µs
Lens		Sigma 50–100 mm f/1.8
Sample		
Material		Steel
Young's modulus	E	190 GPa
Poisson's ratio	ν	0.3
Density	ρ	7923 kg m^{-3}
Thickness	t_S	4.95 mm
Side length	l_s	300 mm
Grid		
Printed grid pitch	p_G	5.89 mm
Grid-sample distance	h_G	1.37 m
Pixels per pitch	ppp	5

for validation testing. Since the test design was symmetric along the vertical axis, the sensors were only placed on one side of the plate, see Fig. 1(d). In addition, a background oriented schlieren (BOS) setup was used between the shock tube exit and test plate as shown in Fig. 1(a). BOS was used to visualize the symmetries of the different blast waves and thus to further validate the pressure reconstruction results. BOS implies that the camera focuses solely on the background, here consisting of a grid pattern. It allows measuring apparent displacements of this background pattern that occur due to changes in the refractive index of light caused by local density gradients in the air between the camera and the background, thus visualizing the position of the blast wave (see *e.g.* [35]). A cross hatched grid with 4 mm printed pitch was used as background pattern and placed perpendicular to the flow direction close to the test section wall. Camera and light source were placed outside of the section and focused on the BOS grid pattern, recording through a section window. Using the same phase detection algorithm as presented in Section 2.2, visualizations of the density gradients that where induced by the approaching blast wave were obtained in terms of apparent displacements of the background pattern.

2.2. Deflectometry

This work applies the load reconstruction methodology introduced in Refs. [29,30], which is limited to small, elastic deformations and thin plate theory. The blast intensities and specimen parameters in the present study are chosen to comply with these limitations, making the deflectometry technique the ideal choice to measure the kinematic fields of interest for the load reconstruction. Deflectometry is an optical full-field measurement technique for the quantification of surface slopes [7]. The measurement approach used in the present study is also explained in Ref. [29] and briefly repeated here. Fig. 3 shows a schematic representation of a typical setup. Deflectometry requires a specimen with specular reflective surface, a cross-hatched grid, a camera and a light source. The camera is placed at an angle next to the printed grid such that it records the reflected grid in normal incidence. Here, the printed grid pitch is denoted as p_G. The angle θ should be minimized to avoid perspective distortions in the recorded image.

Both grid and camera are placed at a distance h_S from the specimen surface. As shown in Fig. 3, a camera pixel records the reflected grid point P when directed at point M on the specimen surface when no load is applied. When the specimen deforms in the out-of-plane direction under an external load, the surface slopes, $d\alpha$, change. The same pixel

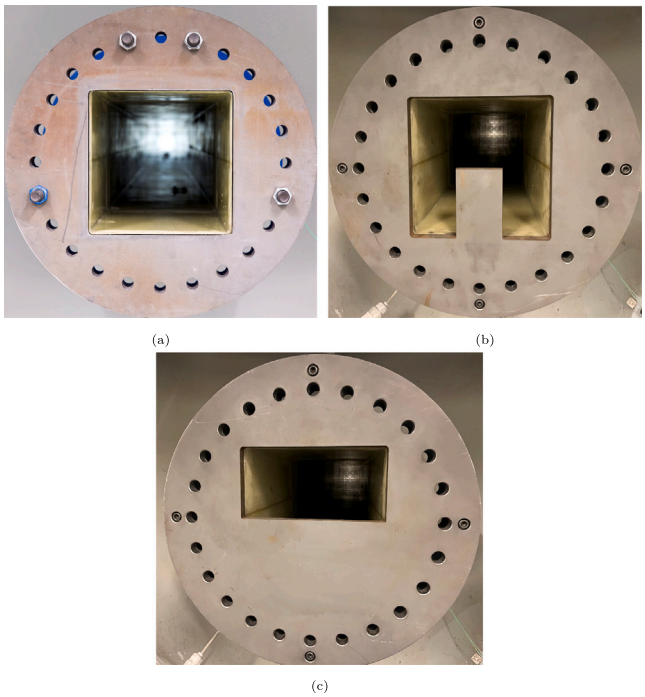

Fig. 2. Pictures of the exit blockages: (a) Unblocked shock tube exit blockage, (b) Column shaped shock tube exit blockage and (c) Half-blocked of unblocked shock tube exit.

directed at point M records the reflected grid point P′ when a load is applied, resulting in an apparent displacement $\boldsymbol{u}$ on the grid. For sufficiently small deflections of the specimen, rigid body movements and out of plane displacements can be neglected.

To quantify the apparent grid displacements that result from applying a load to the specimen, a phase detection algorithm is employed to extract local phase information from grid images. Here, phase detection was done using a spatial phase-stepping algorithm [36,37]. This phase detection algorithm featuring a windowed discrete Fourier transform with triangular weighting was employed as it can suppress some harmonics and errors from miscalibration (see [6,38]. A detection kernel size of two grid pitches was used for this study as it was found to perform well in terms of noise sensitivity and spatial resolution.

The apparent displacement $\boldsymbol{u}$ is then obtained from the difference in phase maps between loaded and unloaded configuration. A linear relation between surface slope changes $d\alpha$ and the displacement $\boldsymbol{u}$ can be derived based on geometrical considerations. Assuming that h_S is large against $\boldsymbol{u}$ and the specimen dimensions, that θ is negligible and that the camera records images in normal incidence, $d\alpha$ can be expressed as (*e.g.* [39]):

$$d\alpha_x = \frac{u_x}{2h_S}, \quad d\alpha_y = \frac{u_y}{2h_S} \quad . \tag{1}$$

2.3. Pressure reconstruction

This subsection briefly introduces the theoretical background and basic principles of the pressure reconstruction approach employed in the present study. Due to the small thickness and small deformations of the test specimen, it is assumed to behave like a thin plate in pure bending. This allows describing the equilibrium of the plate by using the Kirchhoff–Love plate theory. Since the plate material can be assumed as isotropic, homogeneous and linear elastic, the equilibrium equations are expressed by Eq. 2. Here, the surface of the plate is denoted S,

$$\underbrace{\int_S pw^* dS}_{W^*_{ext}} = \underbrace{\rho\, t_S \int_S a\, w^* dS}_{W^*_{inertial}} + \underbrace{D_{xx}\int_S \left(\kappa_{xx}\kappa^*_{xx} + \kappa_{yy}\kappa^*_{yy} + 2\kappa_{xy}\kappa^*_{xy}\right) dS + D_{xy}\int_S \left(\kappa_{xx}\kappa^*_{yy} + \kappa_{yy}\kappa^*_{xx} - 2\kappa_{xy}\kappa^*_{xy}\right) dS}_{W^*_{int}} . \quad (2)$$

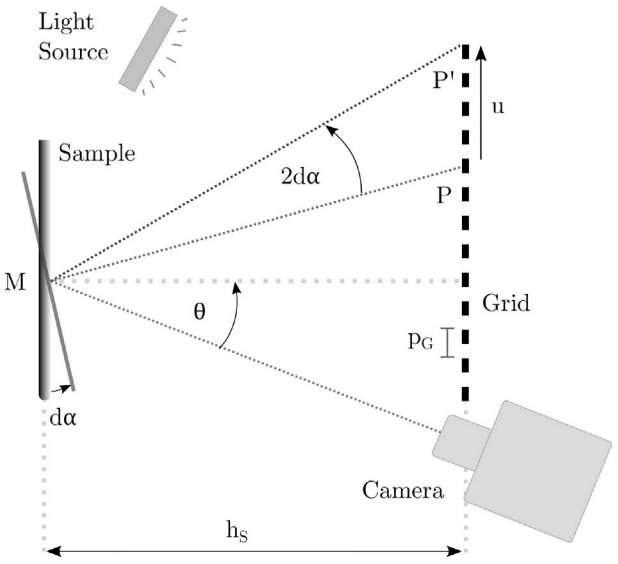

Fig. 3. Top view of deflectometry setup and working principle (redrawn from 29).

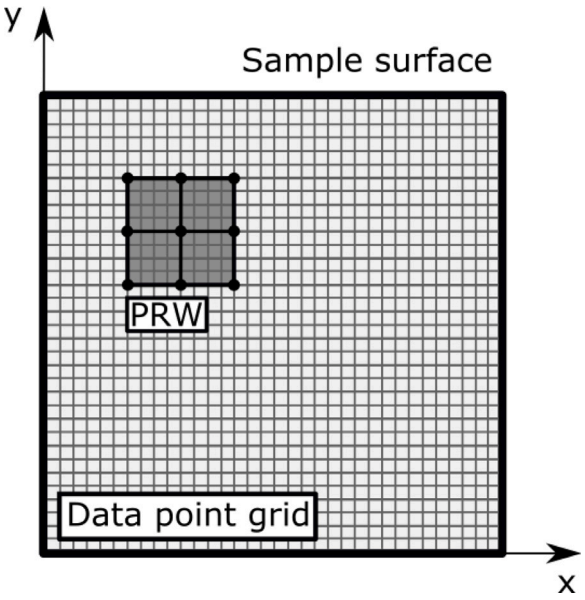

Fig. 4. Sketch of the piecewise pressure reconstruction approach.

the pressure p, the plate bending stiffness matrix components D_{xx} and D_{xy} (due to isotropy, $D_{yy} = D_{xx}$), the surface curvatures κ, the plate material density ρ, the plate thickness t_S, the accelerations a, the virtual deflections w^*, the virtual curvatures κ^*, and the virtual work done by external (W^*_{ext}), inertial (W^*_{int}) and internal ($W^*_{inertial}$) forces. In the present study, the material parameters D_{xx}, D_{xy}, ρ and t_S were known from material calibration *a priori*. κ and a were measured experimentally. The virtual fields w^* and κ^* have to be chosen according to theoretical and practical requirements of the investigated problem like continuity, boundary conditions and sensitivity to noise as explained in detail in the following subsection. In order to obtain spatially resolved pressure information, the investigated surface was divided into subdomains. Pressure is assumed constant over each subdomain, and by shifting the subdomain iterative by one data point in each direction, the entire surface is covered. The subdomain used in this piecewise reconstruction is referred to as pressure reconstruction window (PRW) in the following. Fig. 4 illustrates the approach described above. By approximating the integrals in Eq. 2 with discrete sums, one obtains:

$$\begin{aligned} p = \Bigg(& \rho\, t_S \sum_{i=1}^{N} a^i\, w^{*i} \\ & + D_{xx} \sum_{i=1}^{N} \kappa^i_{xx}\kappa^{*i}_{xx} + \kappa^i_{yy}\kappa^{*i}_{yy} + 2\kappa^i_{xy}\kappa^{*i}_{xy} \\ & + D_{xy} \sum_{i=1}^{N} \kappa^i_{xx}\kappa^{*i}_{yy} + \kappa^i_{yy}\kappa^{*i}_{xx} - 2\kappa^i_{xy}\kappa^{*i}_{xy} \Bigg) \left(\sum_{i=1}^{N} w^{*i}\right)^{-1} , \end{aligned} \quad (3)$$

where N is the total number of discrete surface elements.

2.4. Virtual fields

The virtual fields required for Eq. (3) were defined using 4-node Hermite 16 element shape functions [40]. They yield the required C^1 continuous virtual deflections for obtaining curvatures. Furthermore they allow eliminating the unknown contributions of virtual work over the domain boundaries, because the obtained virtual displacements and curvatures vanish at the borders as all degrees of freedom were set to zero, except for the virtual deflection of the center node, which was set to 1. 9 nodes were defined for each Hermite element in the present study. Fig. 5 shows the virtual fields used in this study. Their complete formulation and an implementation example is given in [32]. The chosen PRW size is an important processing parameter in terms of spatial resolution, noise sensitivity and systematic error. The PRW acts as a low-pass filter, but for large sizes it tends to result in an underestimation of local pressure amplitudes [29]. This is particularly true if the relevant spatial scales of the investigated pressure distribution are small in comparison to the PRW.

2.5. Data processing

This subsection presents the processing steps and techniques that are required to extract curvature and acceleration information from the measured grid images. These fields are required to reconstruct pressure using Eq. (3). To obtain a reference image for the undeformed configuration and to confirm that no major vibrations occurred before impact, a series of grid images were taken starting several hundred frames before the blast wave impacted the test plate. Averaging over a number of these images allowed reducing the noise in the reference image representing the undeformed configuration. The reconstruction steps are outlined in Fig. 6. A phase detection algorithm featuring a triangular window with a width of two grid pitches, here 10 data points, was employed to extract local phase information from the grid images [36]. Every data point was retained, which yields a high data point density. However, this means that 10 neighboring data points in the phase field maps are statistically dependent due to the width of the detection window. Instantaneous slope fields were calculated

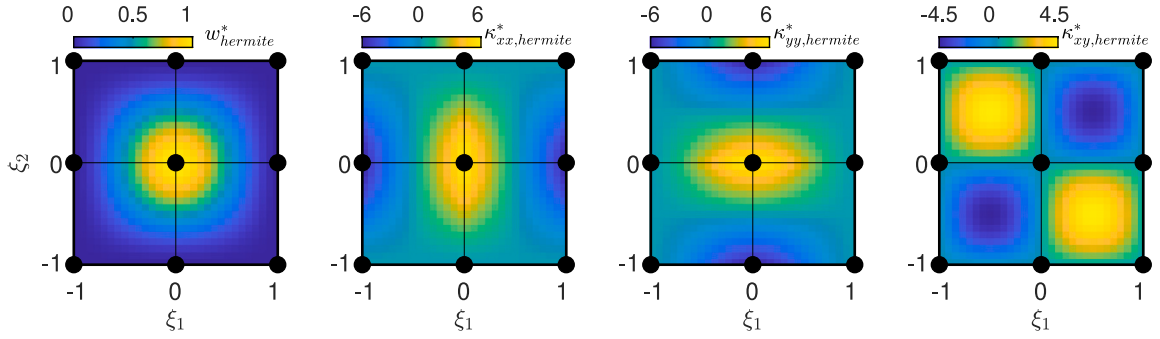

(a) Virtual displacements w^* (b) Transversal virtual curvatures κ^*_{xx} (c) Logitudinal virtual curvatures κ^*_{yy} (d) Twist virtual curvatures κ^*_{xy}

Fig. 5. Example Hermite 16 virtual fields with superimposed virtual elements and nodes (black). ξ_1, ξ_2 are parametric coordinates. The example window size is 30 points in each direction.

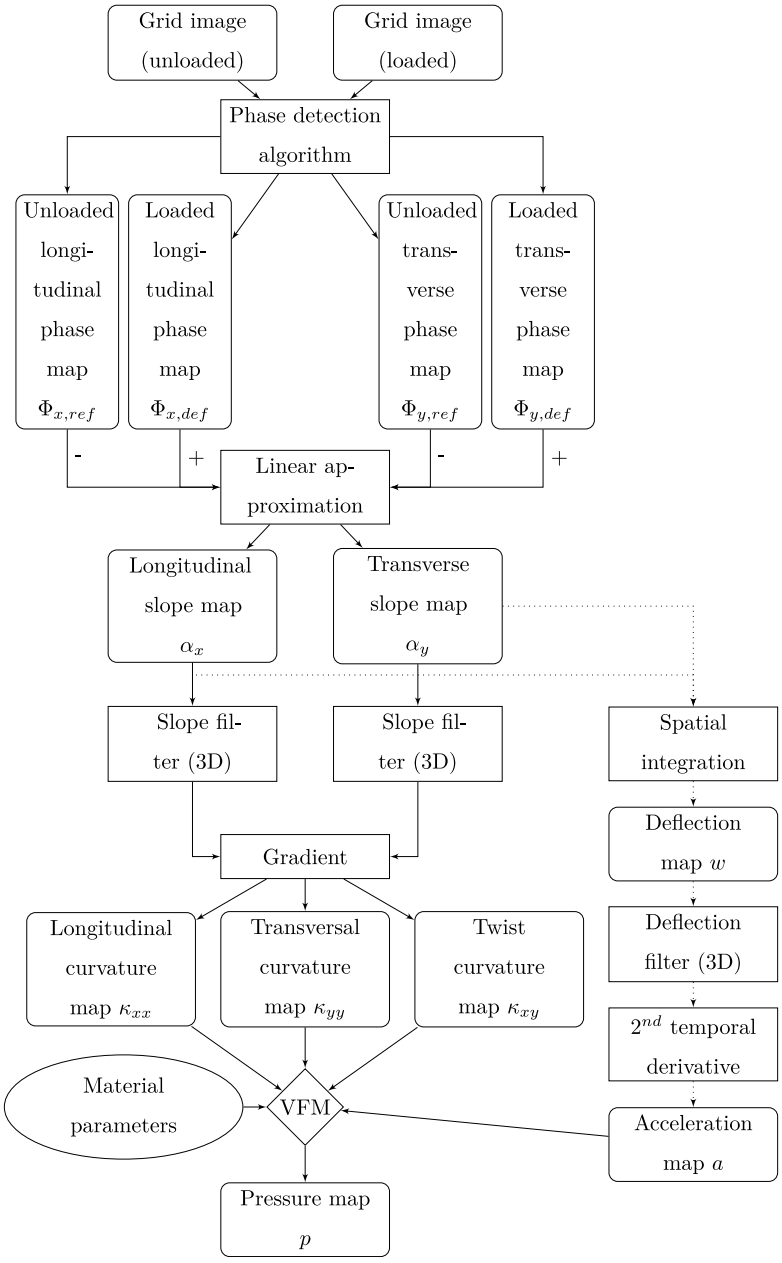

Fig. 6. Data processing steps for reconstruction of quasi static pressure maps from deflectometry measurements.

using phase fields from the unloaded reference configuration and the loaded configuration. Slope fields were filtered using a 3D Gaussian filter with a kernel size of $\sigma_\alpha = 10$ in both spatial dimensions and $2\ \sigma_\alpha$ in time. Here, σ_α denotes the standard deviation of the Gaussian slope filter kernel in terms of data points. This filter was necessary to mitigate noise amplification during spatial differentiation. The filter introduces bias along the boundaries due to its width. The bias has to be removed and thus leads to a loss of $4\ \sigma_\alpha$ data points at each boundary. After filtering, curvatures were determined from the slope maps using a numerical three-point centered finite-difference scheme. Since all data points were retained here, the distance between two data points on the specimen surface is $p_G/10$, assuming that the camera was positioned at the same distance h_S from the specimen surface as the printed grid. The out-of-plane displacements of the plate were obtained from the unfiltered slope fields using a numerical integration approach based on a sparse matrix approximation (see Ref. [41]). This requires knowledge of an integration constant representing the boundary conditions. The integration constant was chosen such that the deflections in the corners of the FOV were zero on average, assuming this to be the correct physical boundary condition. This assumption introduced a potential error which is investigated later in Section 4. Accelerations were obtained from the second temporal derivative of the deflection fields. Pressure was reconstructed using the acceleration, curvatures and material constitutive mechanical parameters as described in Section 2.3. The results were oversampled by shifting the reconstruction window by one data point in both directions until the full field of view (FOV) was covered. A PRW of 30 data points side length was used here.

Pressure transducer measurements were used as reference for evaluating VFM pressure reconstruction results. Transducer measurements allow almost instantaneous pressure readings. In contrast, VFM reconstructions are based on images that were recorded by a camera which integrates over a time interval given by the shutter speed. To emulate the camera integration effect in transducer measurements, transducer data were sampled at 500 kHz and then binned over 5 μs and undersampled to the 75 kHz frame rate of the camera. To allow comparisons to VFM reconstruction results, transducer data were further filtered in time using a Gaussian 1D filter with kernel size $\sigma_t = 2$ to match the deflectometry temporal filter kernel size. An implementation of this processing methodology including load reconstruction is published in [42].

3. Experimental results

This section presents the results from the shock tube experiments. Images were recorded at a frame rate of 75 kHz. Higher frame rates were available but would have resulted in a loss of spatial resolution. 3 repetitions for each exit blockage and 2 repetitions for the open shock tube exit were captured. Section 3.1 presents field maps of the slope, curvature and acceleration fields to demonstrate the deflectometry measurement approach. Section 3.2 first presents the pressure field maps that were obtained for all 3 test cases for different time steps. This is followed by a comparison of the reconstructed pressure at the center point of the plate and the pressure transducer measurements. Finally, reconstructed pressure profiles, pressure transducer measurements and BOS density gradient profiles are compared.

3.1. Kinematic field maps

Figs. 7(a) and 7(b) show representative slope field maps at the time of peak pressure for the unblocked shock tube exit test case. The signal-to-noise ratio is relatively low here, such that noise patterns are clearly visible. Note that the shown instance at 0.2 ms corresponds to the highest reconstructed pressure amplitude, but not the highest recorded slope amplitude. Figs. 7(c)–7(e) show the corresponding curvatures, Fig. 7(f) the deflections and Fig. 7(g) the accelerations calculated from the slope fields. The signal-to-noise-ratio in curvature fields is low for this instance, such that the amplitude of noise patterns are of the order of magnitude of the signal. In contrast, the deflections field shows no visible noise patterns. This can be attributed to the fact that the spatial integration scheme tends to suppress high frequency noise rather than to amplify it like the spatial differentiation scheme does. The peak deflection is approximately 12 μm. The accelerations, which were obtained by means of temporal differentiation, show no visible noise patterns after filtering. Fig. 8 shows field maps for the instance at $\Delta t = 0.3$ ms. There are no visible noise patterns in the slope maps, deflections and accelerations. Curvatures still show some random noise patterns, but the signal amplitude is much higher than observed for the instance at $\Delta t = 0.2$ ms in Fig. 7. To evaluate the relevance of the observed noise patterns on pressure fields, it is useful to consider the different terms describing the virtual work in Eq. 2. Fig. 9 shows the inertial and internal virtual work within the entire field of view normalized by the peak total virtual work, which is the sum of both. The internal virtual work, which depends on the curvatures, is small compared to the inertial virtual work until after the peak amplitude is reached. Since only the internal virtual work is calculated using the curvature fields, this indicates that the overwhelming noise patterns in curvature maps at $\Delta t = 0.2$ ms do not significantly effect the reconstructed peak pressure amplitude.

3.2. Pressure distributions determined using VFM

Fig. 10 shows full-field pressure reconstructions for the open shock tube exit case as well as interpolated pressure transducer measurements. Note that the white markers indicate the positions of the pressure transducers. Pressure transducers are well established for accurate pressure amplitude measurements, but the limited number of sampling points on the specimen only allow a rough estimation of the pressure distribution. The shape of the observed pressure distribution in transducer data approximately resembles a bi-axial half sine wave with initially increasing and later decreasing amplitude. The VFM pressure reconstruction results agree well with this shape within the more limited field of view, but the peak amplitude is 18% lower than in transducer measurements. Fig. 11 shows the comparison between results from both pressure measurement approaches for the half-blocked shock tube exit case. The pressure distributions agree qualitatively well between transducer measurements and VFM reconstructions for all presented instants. The shape of the pressure distribution differs significantly from the unblocked case and shows a lower peak amplitude. The initial blast wave impact at $\Delta t = 0.15$ ms on the test plate shows a pressure peak in the top half of the field of view. In the following instances at $\Delta t = 0.2$ ms and $\Delta t = 0.25$ ms the peak pressure region shift down in negative y-direction at decreasing amplitude. The observed peak amplitude in the VFM reconstructions is approximately 13% lower than that in the transducer data. Fig. 12 shows the results for the third test configuration with a column shaped nozzle exit blockage. Both VFM reconstruction and transducer data show that the initial blast wave impact occurs at the top of the field of view. The peak pressure amplitude increases and shifts towards the center of the plate at $\Delta t = 0.2$ ms and decreases at $\Delta t = 0.25$ ms. The peak pressure amplitude determined using the VFM is approximately 13% lower when compared to the corresponding transducer data.

Fig. 13 shows comparisons of pressure transducer measurements and VFM pressure reconstructions at the center of the test plate. Both raw and processed transducer data are presented. As already mentioned in Section 2.5, the transducer data were processed to match the effects of camera integration time and of the filters that were used on deflectometry data before VFM reconstructions. The effect of these processing steps is evident by comparing the raw and processed transducer data in Fig. 13, which shows that binning and filtering increase the pressure rise time and decreases the peak amplitude significantly. The filtered transducer measurements are therefore used as basis of comparison and

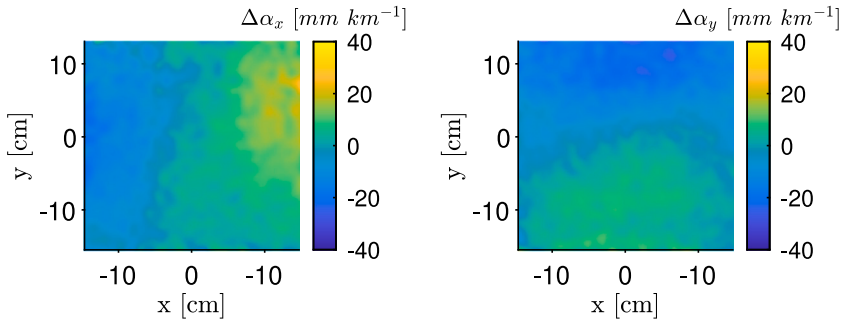

(a) Transverse slopes.

(b) Longitudinal slopes.

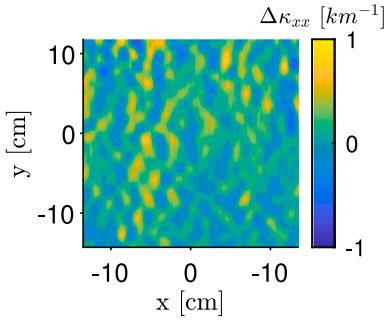

(c) Transverse curvatures.

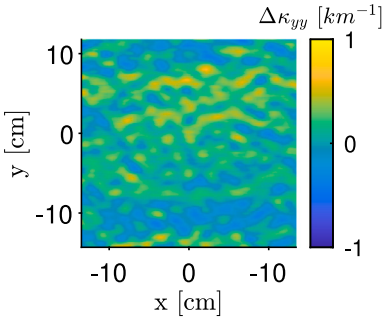

(d) Longitudinal curvatures.

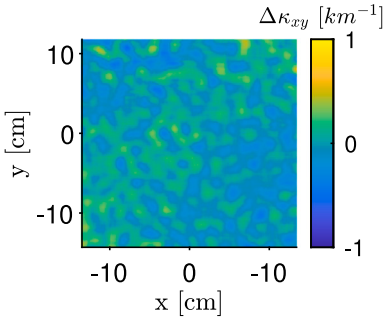

(e) Twist curvatures.

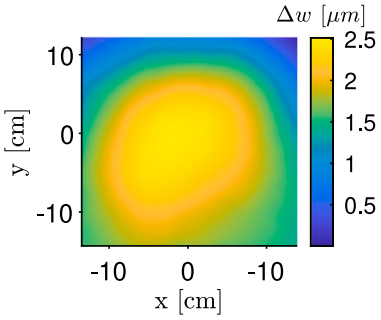

(f) Deflections.

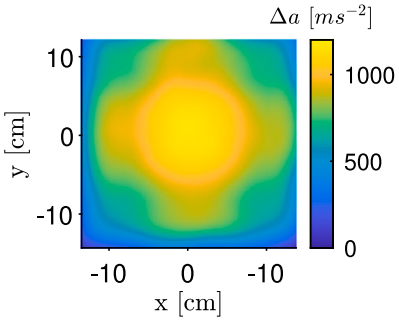

(g) Accelerations.

Fig. 7. Instantaneous field maps from experimental measurements at $\Delta t = 0.2$ ms for open nozzle exit test case.

to evaluate the performance of the VFM in reconstructing the pressure in the following.

The VFM data show a repeatability of the reconstructed peak pressure amplitude between the runs to within approximately 4% for all test configurations. The open nozzle exit test case shown in Fig. 13(a) confirms the discrepancy in peak amplitude between transducer data and VFM reconstructions that was also observed in the field maps. Despite the difference in amplitude, the qualitative time histories of the curves are similar for both VFM reconstruction and transducer data. After approximately $\Delta t = 0.3$ ms the VFM results become increasingly noisy and repeatability decreases due to the higher relative contribution from the noisier curvatures. Fig. 13(b) shows the comparison of transducer data and VFM reconstructions for the half-blocked exit test case. The observed peak amplitude is significantly lower in this test than in the unblocked exit configuration. Further, the agreement between VFM and transducer data is better as was also found in the field maps. Fig. 13(c) shows the center point pressure comparison for the column shaped exit blockage tests. Here, the repeatability of VFM pressure reconstruction results is good even until well after the peak pressure amplitude is reached. While the pressure amplitude from VFM data is still underestimated when compared to transducer data, the shape of the pressure curves agree qualitatively well up to approximately $\Delta t = 0.3$ ms. After $\Delta t = 0.55$ ms VFM data show an overestimation of the transducer pressure amplitude, likely due to an increasing influence of vibrations in the setup at this time instance.

Visualizing the approaching blast waves in front of the test plate using BOS allows an additional, qualitative validation of the pressure distribution shapes identified in the VFM reconstructions. Due to the previously mentioned boundary-induced bias in the grid method, visualizations at distances closer than 4 mm of the test plate were not possible here. Fig. 14 shows BOS measurements of the apparent grid displacement induced by the blast wave for the open nozzle exit case, as well as center line pressure values from both VFM reconstructions and filtered transducer data at 4 time instances. Note that the rise in pressure amplitude observed before the shock front reaches the test plate is due to the 3D filter, which blurs the data in both space and time. The blast front appears planar in the center region with increasing backwards curvature towards the top and bottom. The grid displacement measured using the BOS grid in the background is highest in the center and decreases towards the top and bottom. This indicates a varying

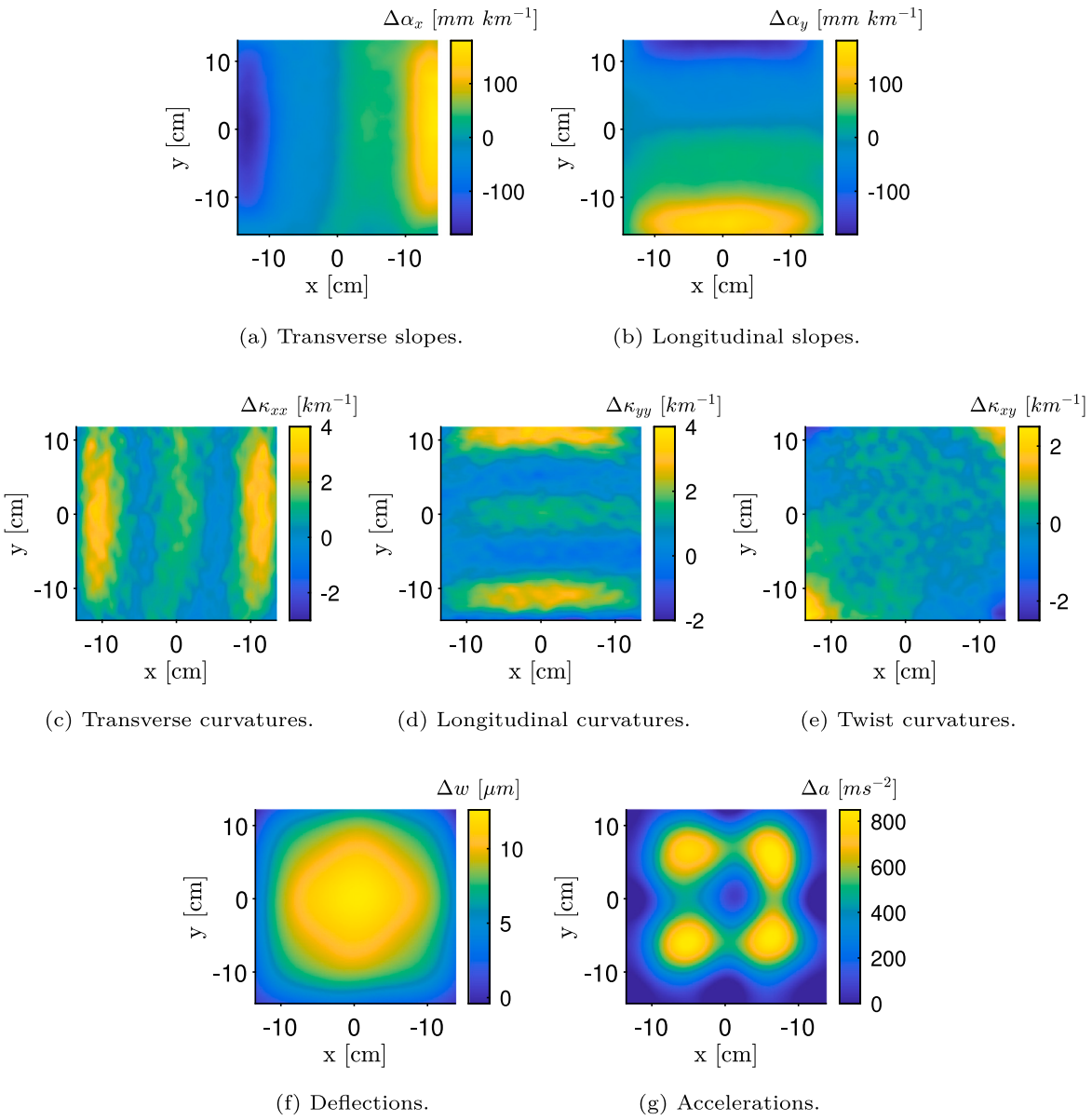

(a) Transverse slopes. (b) Longitudinal slopes.

(c) Transverse curvatures. (d) Longitudinal curvatures. (e) Twist curvatures.

(f) Deflections. (g) Accelerations.

Fig. 8. Instantaneous field maps from experimental measurements at $\Delta t = 0.3$ ms for open nozzle exit test case.

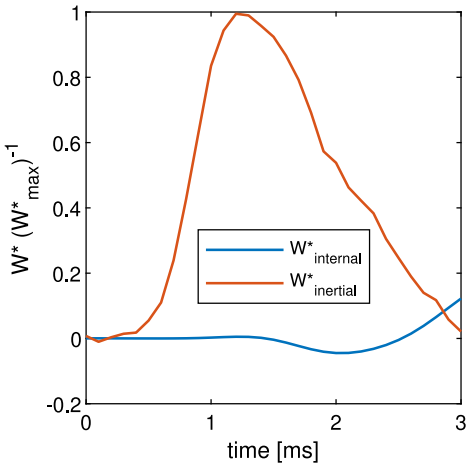

Fig. 9. Normalized virtual work components within the field of view for open nozzle exit test case.

blast intensity consistent with the observed, approximately half-sine shaped pressure distribution during the blast–structure interaction. The peak amplitudes of the reconstructed pressures are lower than those seen in transducer data. At some distance from the plate center the pressure values show better agreement. Fig. 15 shows the same plots for the half-blocked exit case. The blast front has a strong curvature and approaches the test plate from the top half of the field of view. The position, shape and intensity of the blast wave are consistent with the distributions identified in both the transducer and reconstructed pressure data. Fig. 16 shows the BOS and pressure measurement results for the column shaped exit blockage case. The blast wave shows a more complex shape that appears to have three pressure fronts that are visible in the BOS visualization. One pressure front is similar in shape to the front formed in the open exit case, but with lower intensity and thickness. The second front has a similar shape and appears to follow the first at a small vertical angle at $\Delta t = 0.0$ ms and appears to overlap with the first front upon reaching the plate specimen. The third front resembles the shape observed in the half-blocked exit case at lower intensity. Consequently the pressure history along the center line shows a more complex behavior than the previous cases. The pressure rises

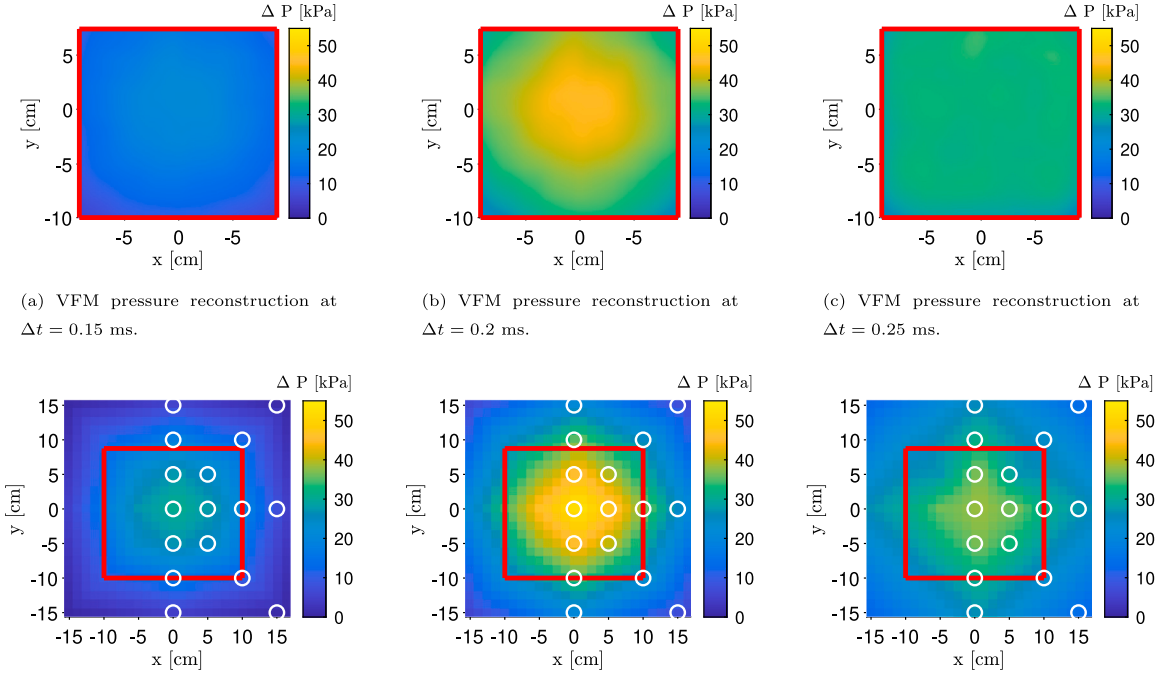

(a) VFM pressure reconstruction at $\Delta t = 0.15$ ms.

(b) VFM pressure reconstruction at $\Delta t = 0.2$ ms.

(c) VFM pressure reconstruction at $\Delta t = 0.25$ ms.

(d) Interpolation of pressure transducer data at $\Delta t = 0.15$ ms.

(e) Interpolation of pressure transducer data at $\Delta t = 0.2$ ms.

(f) Interpolation of pressure transducer data at $\Delta t = 0.25$ ms.

Fig. 10. Pressure field maps for open nozzle exit test case.

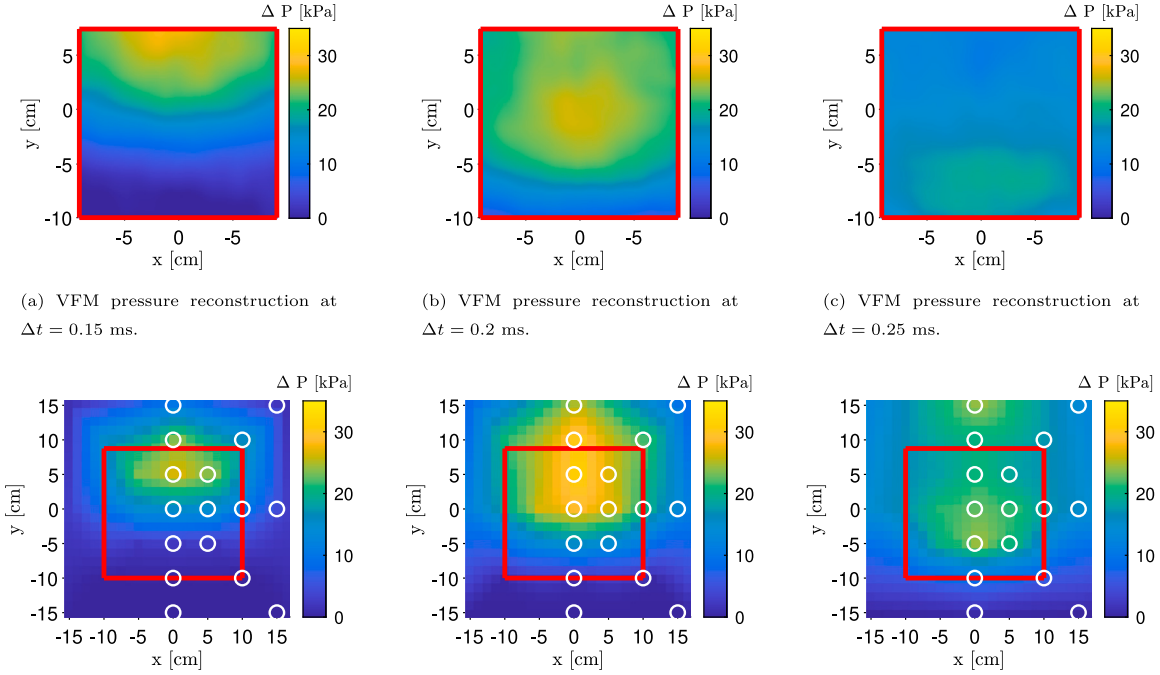

(a) VFM pressure reconstruction at $\Delta t = 0.15$ ms.

(b) VFM pressure reconstruction at $\Delta t = 0.2$ ms.

(c) VFM pressure reconstruction at $\Delta t = 0.25$ ms.

(d) Interpolation of pressure transducer data at $\Delta t = 0.15$ ms.

(e) Interpolation of pressure transducer data at $\Delta t = 0.2$ ms.

(f) Interpolation of pressure transducer data at $\Delta t = 0.25$ ms.

Fig. 11. Pressure field maps for half-blocked nozzle exit test case. Transducer data filtered in time with kernel $\sigma_t = 2$ to match deflectometry temporal filter kernel size.

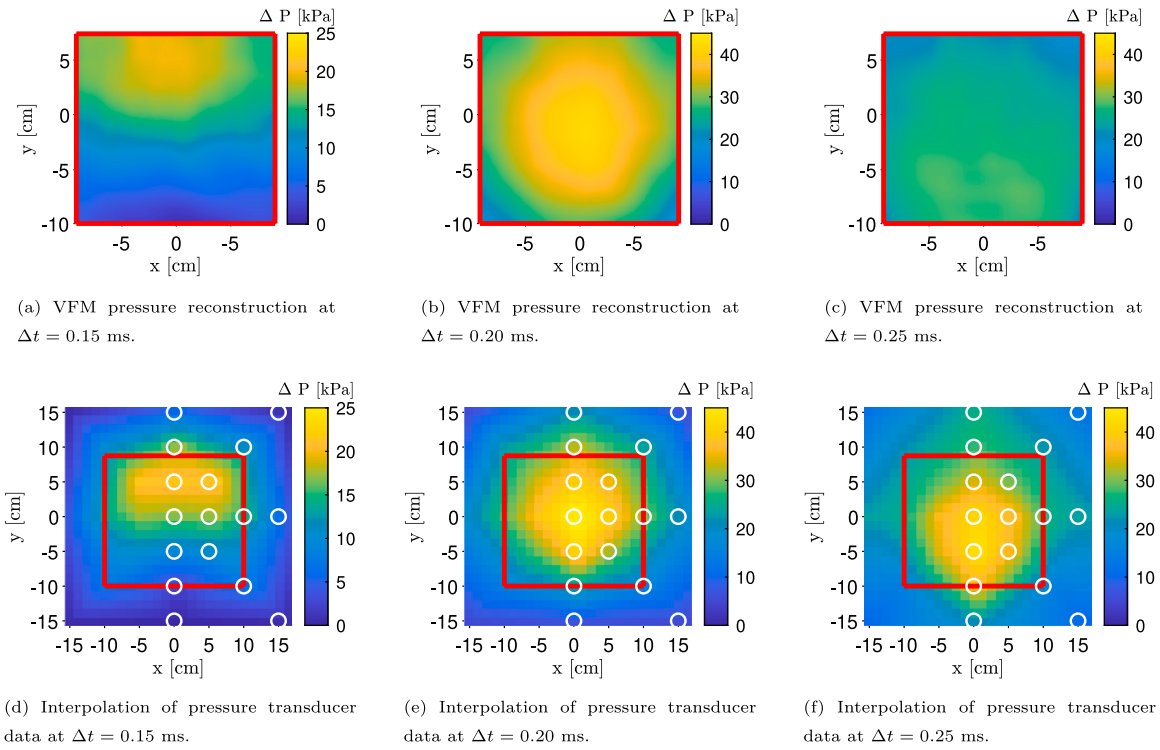

(a) VFM pressure reconstruction at $\Delta t = 0.15$ ms.

(b) VFM pressure reconstruction at $\Delta t = 0.20$ ms.

(c) VFM pressure reconstruction at $\Delta t = 0.25$ ms.

(d) Interpolation of pressure transducer data at $\Delta t = 0.15$ ms.

(e) Interpolation of pressure transducer data at $\Delta t = 0.20$ ms.

(f) Interpolation of pressure transducer data at $\Delta t = 0.25$ ms.

Fig. 12. Pressure maps for column shaped blockage nozzle exit test case.

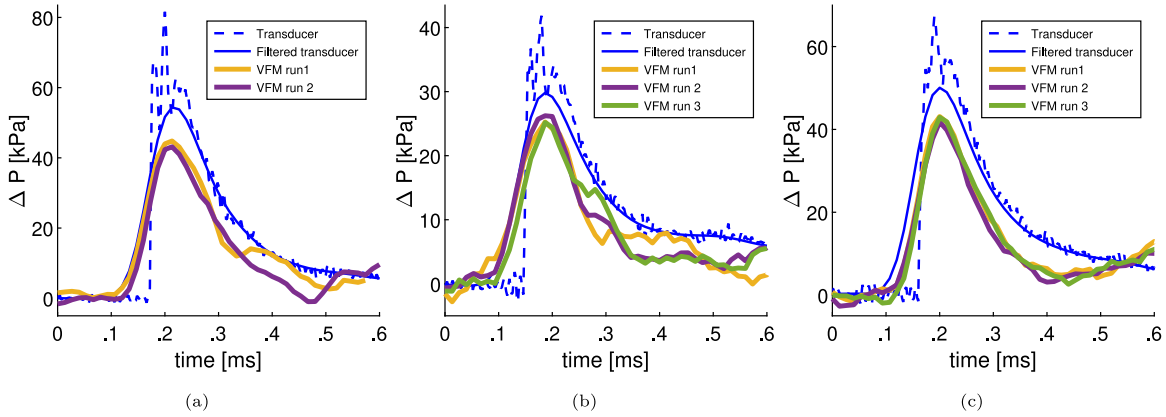

(a) (b) (c)

Fig. 13. Comparison of filtered and raw pressure transducer measurements and VFM pressure reconstructions at the center point of the test plate. Transducer data filtered in time with kernel $\sigma_t = 2$ to match deflectometry temporal filter kernel size. Pressure histories at center point for (a) open nozzle exit, (b) half-blocked nozzle exit and (c) column shaped blockage at nozzle exit.

first in the top half of the test plate and the position of the pressure peak propagates in negative y-direction at increasing amplitude. Transducer data and VFM reconstruction results agree qualitatively well, but the measured amplitudes in reconstructed pressures are lower.

Motivated by the discrepancies between transducer data and VFM reconstruction results, an error assessment based on synthetic data to investigate possible error sources is presented in the following section.

4. Analysis of error sources by virtual experiments

Virtual experiments were carried out to assess the accuracy of the pressure reconstruction methodology, providing strict control of the input and without the physical limitations related to the experimental setup in Section 3. The aim of the accuracy assessment is not to reproduce the physical experiments exactly, but to highlight the relative influence of different error sources present in the physical experiments. Special focus is placed on the influence of the limited field-of-view and filtering of kinematic fields. The virtual experiments were performed similarly as in Ref. [43]. The work flow is illustrated in Fig. 17 and consists of the following steps:

1. Determine the deformation fields for a given pressure distribution using finite element analysis (FEA).
2. Approximate inter-nodal deformations by interpolation.
3. Generate grid images corresponding to the deformation fields.
4. Average grid images in time to account for a finite shutter speed.
5. Add camera sensor noise to the grid images.

The virtual experiments were performed using Abaqus™ Explicit, which allowed obtaining the nodal deflection of a thin plate exposed to a predefined spatio-temporal pressure distribution. The plate was modeled with the same dimensions and material properties as used in the physical experiments (see Table 1). The modeled square plate was discretized using S4R shell elements with a side length of 4.69 mm,

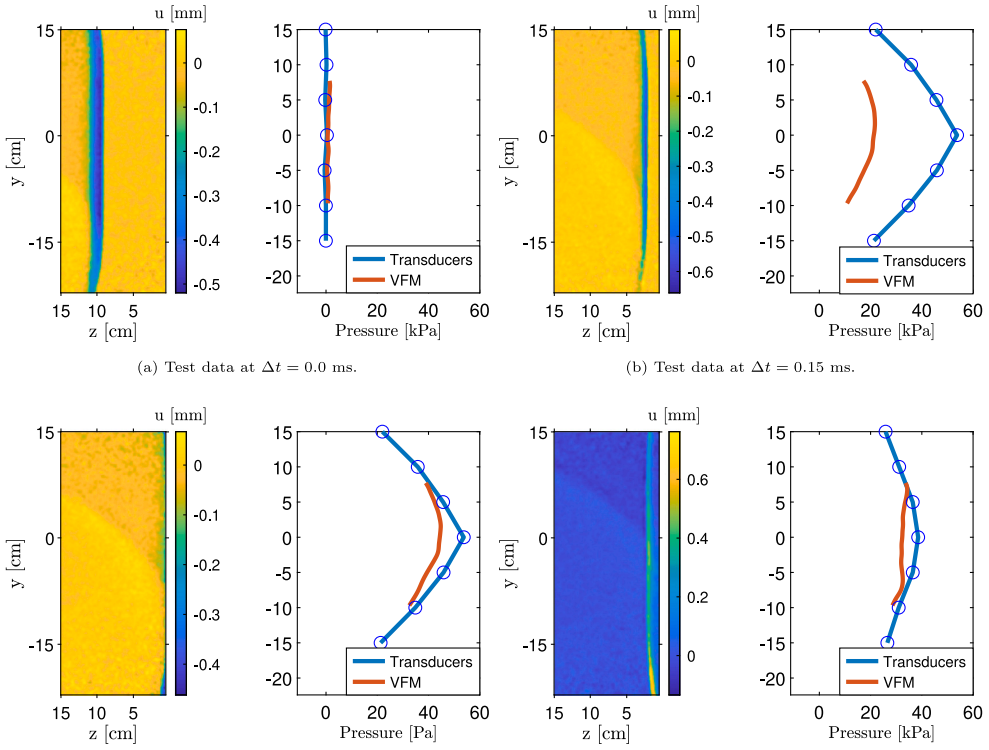

(a) Test data at $\Delta t = 0.0$ ms.

(b) Test data at $\Delta t = 0.15$ ms.

(c) Test data at $\Delta t = 0.2$ ms.

(d) Test data at $\Delta t = 0.25$ ms.

Fig. 14. Apparent grid displacements measured using BOS visualization of approaching blast wave (left) and pressure along the center line of the test plate (right) at different time steps. Open shock tube exit test case.

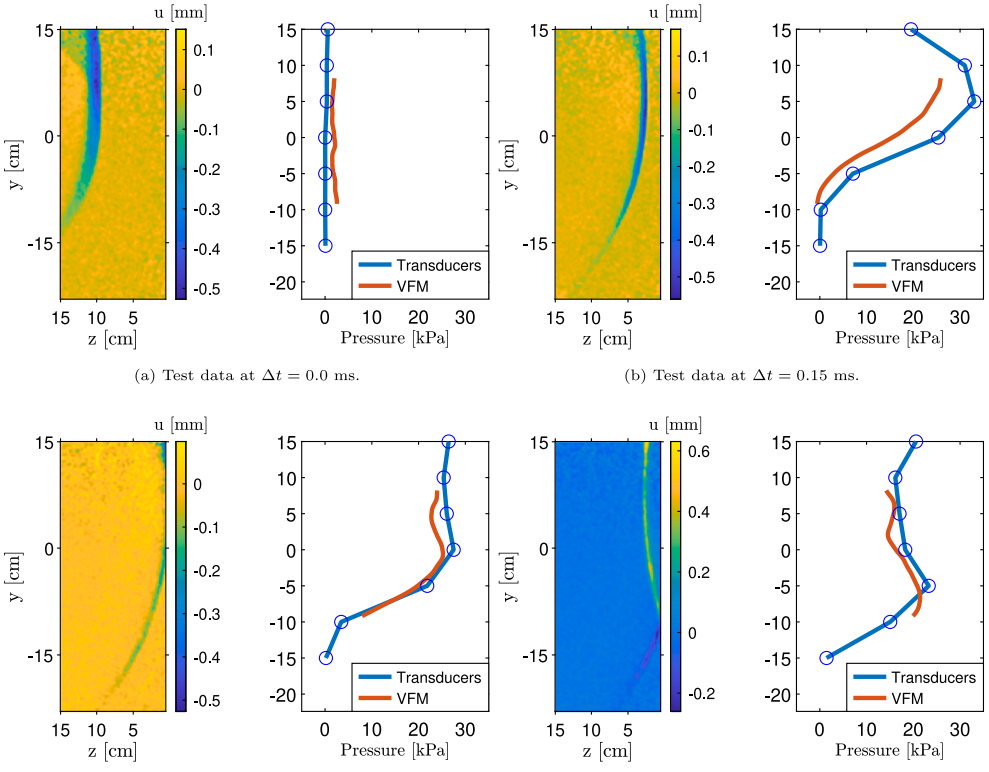

(a) Test data at $\Delta t = 0.0$ ms.

(b) Test data at $\Delta t = 0.15$ ms.

(c) Test data at $\Delta t = 0.2$ ms.

(d) Test data at $\Delta t = 0.25$ ms.

Fig. 15. Apparent grid displacements measured using BOS visualization of approaching blast wave (left) and pressure along the center line of the test plate (right) at different time steps. Half-blocked shock tube exit test case.

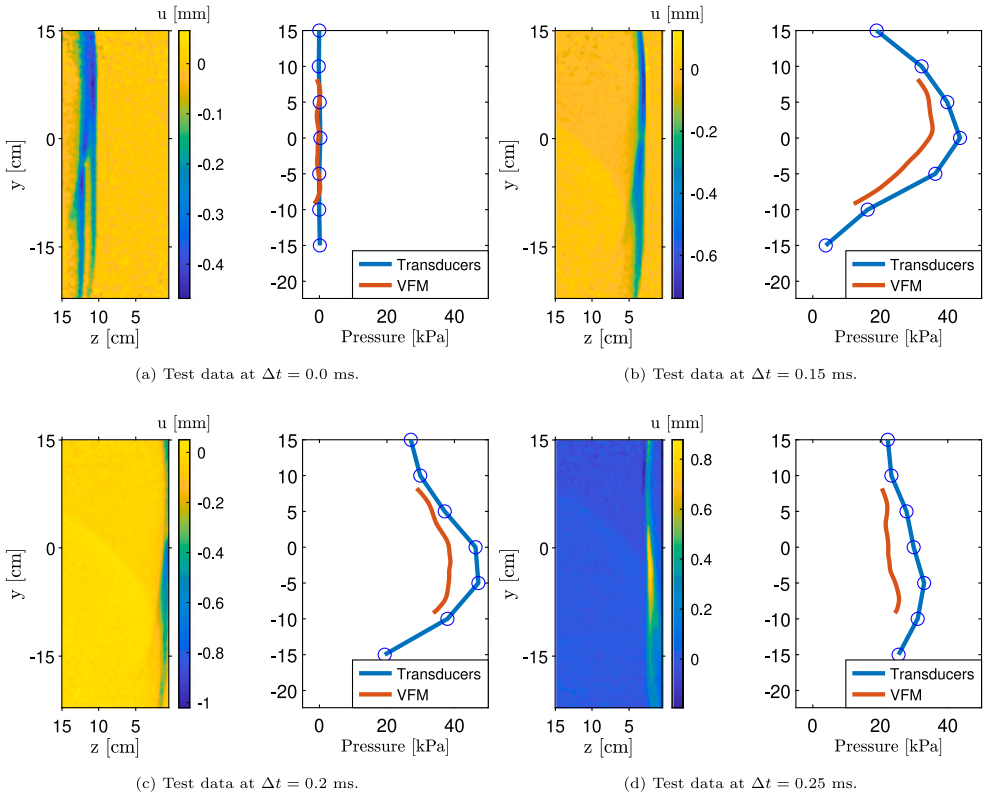

(a) Test data at $\Delta t = 0.0$ ms.

(b) Test data at $\Delta t = 0.15$ ms.

(c) Test data at $\Delta t = 0.2$ ms.

(d) Test data at $\Delta t = 0.25$ ms.

Fig. 16. Apparent grid displacements measured using BOS visualization of approaching blast wave (left) and pressure along the center line of the test plate (right) at different time steps. Column shaped shock tube exit blockage test case.

allowing the nodal deformation field to be sampled on a 64 × 64 point grid. The outer boundaries of the plate were constrained against both translation and rotation, mimicking the constraints imposed by the fixture used in the physical experiments. A generic pressure distribution based on the open-channel physical experiments was applied to the surface of the plate and is described by:

$$p(x, y, t) = A(t)(sin(\pi x l^{-1}) + sin(\pi y l^{-1})), \tag{4}$$

where x and y are the spatial coordinates of the plate surface and $A(t)$ is the peak pressure amplitude. This 2D, half-sine shaped distribution was chosen as it resembles the shape of the physical pressure distribution of the non-blocked nozzle exit test case and thus a qualitatively comparable spatial pressure distribution. To highlight the effect of frame rate and filtering of the kinematic fields in time used in the pressure reconstruction, a peak pressure amplitude A was defined as a time-series with a sampling rate of 500 kHz (i.e., the same frequency as in the transducer measurements in Section 3). The peak pressure amplitude was extracted from the transducer measurements without exit blockage (see Fig. 13(a)) in order to obtain a comparable loading amplitude in the simulation. The nodal deflection fields were interpolated using bi-cubic splines, allowing the deflection fields to be sampled for 512 × 512 data points, emulating the number of pixels on the camera sensor. The grey scales of the artificial grid were modeled by a periodic function with a wavelength corresponding to the experimental grid pitch, similar to the approach described in Ref. [43]. Deformed grid images were generated using Eq. (1) based on the deflection fields determined from the FEA and used as input for the pressure reconstruction. The finite exposure time of the camera used in the physical experiments was emulated in the virtual experiments by generating images corresponding to a sampling rate of 750 kHz and calculating the pixelwise mean along the time axis for four images. This results in a frame rate of 75 kHz and an exposure time of 5.33 µs. Camera sensor noise was added to the grid images as additive Gaussian noise, determined from 20 reference images. The standard deviation of the Gaussian noise was found to be 0.8% relative to the span of grey-scale values in the image. It should be noted that camera noise is added on top of the temporal noise that is contained in the transducer data, which are used as input to this simulation. The grid images were used as input to the pressure reconstruction analysis, and the same pressure reconstruction processing parameters as used for the physical experiments were employed.

A reconstruction of noise-free simulated data with the same sample rate as transducer data is shown for reference in Fig. 18. It captures the peak amplitude of the input pressure to 98% and reproduces even oscillating temporal features. The small underestimation is a result of the 5-point central difference scheme that is used to obtain accelerations from deflection fields and of the spatial filtering effect of the PRW used in the pressure reconstruction. The good agreement between input pressure and reconstructed pressure from noise-free kinematic fields at high sample rate is an important finding, demonstrating that the VFM pressure reconstruction approach itself performs well. This builds confidence in the fact that the virtual experiments can be used to study the influence of signal-to-noise ratio and the effect of a limited field of view (FOV). Since the reconstruction is conducted on full-field data, albeit simulated, this further shows that it is possible to capture the steep pressure rise time experimentally if cameras with sufficiently high frame rate and spatial resolution are available.

Fig. 18 shows the influence of the spatial and temporal filter kernel size on the reconstructed pressure from the virtual experiment. Noise removal by employing spatial and temporal filters is necessary to obtain reconstructed pressures with an acceptable noise level. However, the exact influence of these filters on the reconstructed pressure amplitude is not known *a priori*.

The noise level of the reconstructed pressure from noisy kinematic fields is highly influenced by the size of the temporal and spatial filter kernel sizes. For the smallest filter kernels, the noise level of the mid-point pressure can be close the input peak pressure amplitude due to the pronounced noise patterns. However, when the size of the filter kernels are increased, the noise level decreases and shows close correspondence

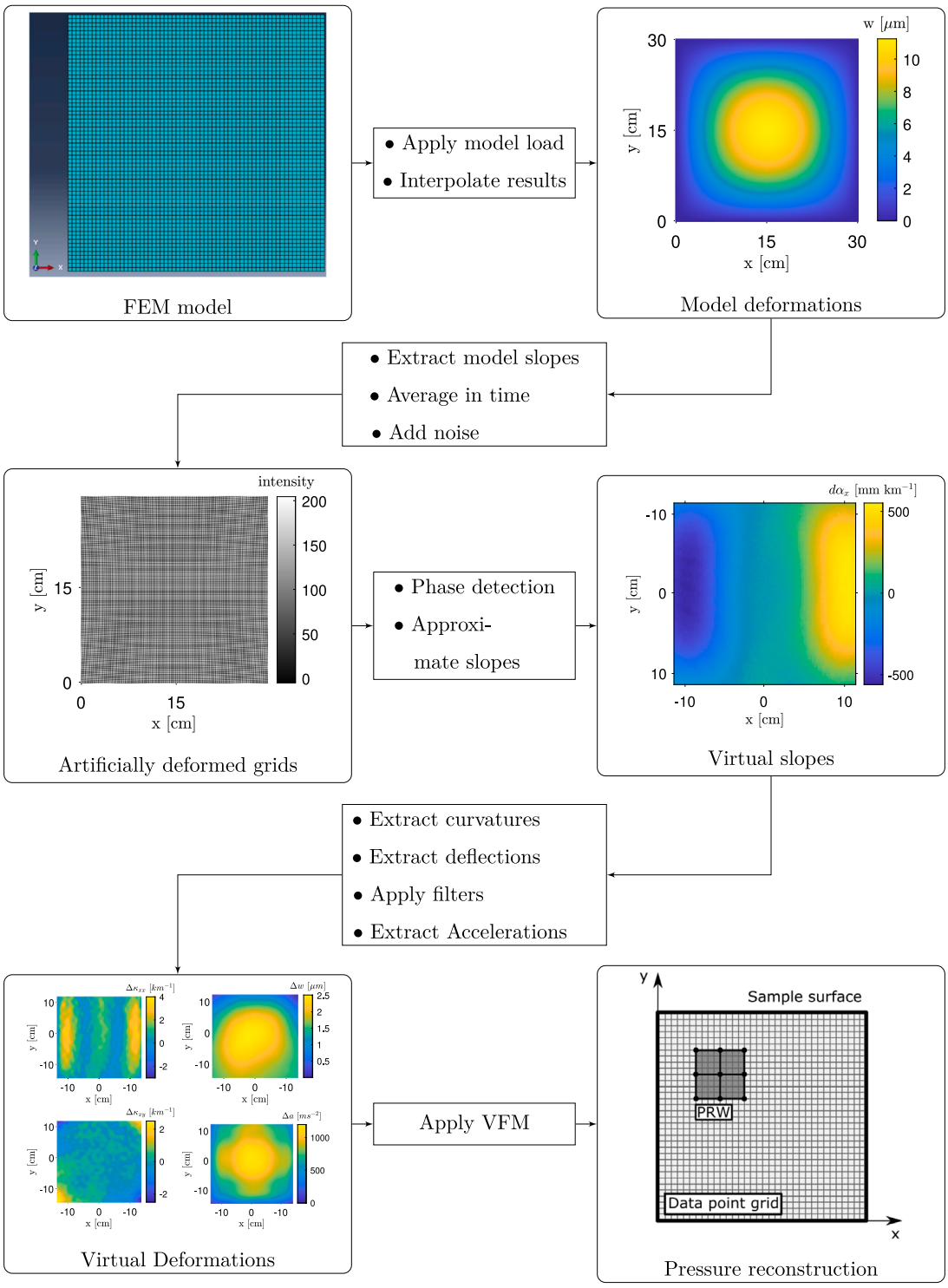

Fig. 17. Flow diagram of virtual experiment approach.

to the filtered input pressure signal. The temporal filter kernel size shows a more pronounced effect on the peak amplitude than the spatial kernel size. This can be attributed to the observation that in the present case the acceleration-dependent inertial virtual work has much larger amplitudes than the internal virtual work.

To investigate the influence of limited field of view (FOV), a given number of pixels around the edges of the grid image were removed before the pressure reconstruction. This is relevant because it influences the accuracy of the assumption that the integration constant used when calculating deflections from the slope fields does not change over time. Any errors in this assumptions made for determining the integration constant can influence the accuracy of acceleration and pressure amplitudes as they are obtained from these deflection measurements. The reconstructed pressure in the mid-point of the plate is shown in Fig. 19 for different levels of FOV reduction. The reconstructed peak pressure decreases notably as the FOV is reduced by more than 40 points. This shows that it is important to retain the data along the approximately undeformed edges. In the present case this means that the spatial filter should not be applied to slope fields but to deflection fields, avoiding the loss of data points along the edges before integration.

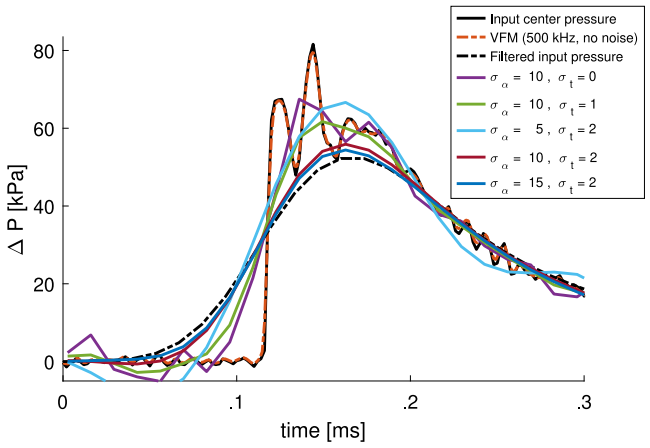

Fig. 18. Reconstructed pressure at the middle of the plate for different spatial filter kernel sizes. The pressure applied to the plate is included for reference.

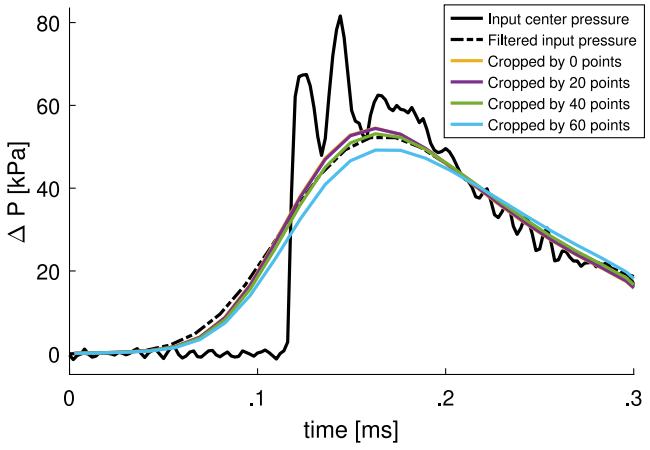

Fig. 19. Reconstructed pressure at the middle of the plate for different field of views reduction. The pressure applied to the plate is included for reference.

Overall, pressure reconstructions of simulated data agree much better with the input pressure than the reconstructions of experimental data do with the transducer measurements (see Fig. 13(a)). This issue is discussed in the following section.

5. Discussion

The work presented in Sections 3 and 4 can be summarized as follows:

1. A qualitative comparison of pressure distributions and histories obtained from pressure transducer data and from reconstructions performed on optical measurements. Distributions were found to compare well between both methods.
2. A quantitative comparison of transducer data and reconstructed pressure values at the center point of the investigated test plate area over time. Underestimations of up to 18% were observed for the reconstructed pressure amplitude when compared to transducer data.
3. A quantitative comparison of transducer data and reconstructed pressure values obtained along a line through the center of the test plate. The underestimations observed from the center point comparison were confirmed.
4. A qualitative comparison of the measured pressure values obtained along a line through the center of the test plate with the shape of the incoming shock wave visualized using BOS. The changes observed in the pressure distribution over time were found to agree well.
5. A simulation of both the plate bending behavior using a generic but comparable loading case and the optical experiment to demonstrate the performance of the approach and investigate error sources. Several critical experimental and processing parameters were identified this way.

The presented results demonstrate the applicability of combined optical deformation measurements and VFM pressure reconstruction for determining full-field, time-resolved surface pressure distributions in a blast loading environment. Comparisons of the VFM pressure reconstructions with pressure transducer measurements demonstrated good qualitative agreement of the pressure distributions. The rise times identified in VFM reconstructions agree well with those found in filtered transducer data. However, due to the limited frame rate of the camera and the required temporal low-pass filter, the optical approach could not capture the steep rise time that was measured in raw transducer data. In order to achieve the high temporal resolution that is required for capturing blast events more accurately, cameras with higher frame rates, the same or a higher number of pixels and a similar or better signal-to-noise-ratio are required. As the pressure reconstruction based on the simulated data show in Fig. 13(a), the VFM approach can capture the steep pressure rise time when a sufficient frame rate is available.

Pressure amplitudes in VFM reconstructions were found to be lower than in transducer measurements, motivating virtual experiments to assess potential error sources and processing bias. Two dominant error sources were identified and assessed in the virtual experiments, being loss of data points around the boundaries of the slope fields and the use of low-pass filters to reduce the noise level of the kinematic fields. Some loss of data points could not be avoided here due to shadows from the aluminum frame fixing the specimen, and phase detection bias around the edges.

In the present study, both bias around the edges from the phase detection algorithm and shadows from the frame fixing the test plate caused loss of information around the edges. When data points are missing around the edges of the slope fields, the correct deflection field is not necessarily obtained from integration of the slope field. When the deflections of the corners are non-zero, a key assumption made for the integration boundary conditions is violated, namely that the deflections in the corners are negligible. This assumption is less accurate the further one moves away from the constrained edges of the plate. As the acceleration fields are calculated from the deflection fields by differentiation in time, also the acceleration fields may contain bias due to inaccurate boundary conditions. The virtual experiments demonstrate that for a plate with fully clamped boundaries around the edges and a spatial pressure distribution represented by a half-sine wave, a significant loss of data points along the edges is tolerated before pronounced reductions of the reconstructed pressure amplitude is observed. As the deflection of the plate is in the order of micrometers (μm) at peak pressure. These very small deformations combined with possible inaccuracies in the fixture used to clamp the plate imply that deflection and rotation could be present at the edge of the plate. If deflections or rotations of the plate are present in the corners of the plate, the boundary conditions implicitly imposed by the integration constant are violated, directly affecting the reconstructed pressure. To avoid this issue, it was attempted to determine the integration constant by measuring the deflection of a single point directly using a laser, but due to the limited deflection resolution of the laser and vibrations in the shock tube no usable results were obtained. Another possible error source are vibrations of camera and grid during the experiment. However, the good repeatability of the optical measurements up to 0.05 ms after peak pressure indicates that this error is smaller than 5% up to that time instance.

Previous studies have found that noise in the kinematic fields, filtering of the kinematic fields and VFM processing can lead to both

over- and underestimation of the pressure amplitude, depending on the noise level, spatial and temporal resolution and the processing parameters (see Ref. [29]). Noise mitigation by low-pass filtering reduces the spectral content of the kinematic fields, but tends to reduce the reconstructed pressure amplitude. Overall, the good qualitative performance of the approach in identifying blast wave distributions on the impacted plate offers new opportunities for the research on blast–structure interactions during the dynamic response of thin steel plates.

6. Concluding remarks and outlook

This study explores a novel load reconstruction methodology to quantify the governing surface pressures acting on thin steel plates in pure, elastic bending during the blast–structure interaction in shock tube tests. Non-intrusive, full-field deformation measurements were carried out using a deflectometry setup to measure the plate dynamics. Full-field surface pressures were then reconstructed using the principle of virtual work, where inertial and internal virtual work were calculated based on the deformation measurements. Nearly non-deformable plates equipped with pressure transducers were also used to obtain reference measurements for validation of amplitudes and time histories. BOS measurements were carried out to evaluate the blast wave shapes and the pressure wave dynamics. Virtual experiments were carried to evaluate the performance of the load reconstruction methodology, without the physical limitations impose by the experimental setup. The main conclusions from the study are as follows:

- VFM pressure reconstructions were found to capture the spatial pressure distributions and dynamics qualitatively well. However, peak pressure amplitudes were up to 18% lower than in transducer data. The virtual experiments indicate that this discrepancy is likely the result of ill-defined boundary conditions in the spatial integration of experimental data. Despite the observed underestimation of the pressure amplitude, the method is a promising addition to available pressure measurement approaches in blast environments.
- The main advantages of pressure reconstruction from optical deformation measurements are the possibility for non-intrusive measurements and the high data point density. The resolution in time depends on available imaging equipment and will improve with the availability of faster high-resolution cameras. Improvements in other measurement techniques like 3D-DIC and an extension of the VFM pressure reconstruction framework beyond the thin-plate assumption may allow pressure reconstructions in a wider range of applications in the future.
- The proposed load reconstruction methodology can amend traditional techniques using transducer and load cell measurements in providing information which was previously considered as inaccessible. To improve the quality and applicability of the method, future work will focus on load reconstruction on test samples that are subject to larger deformations. Thus, the proposed methodology has the potential of being a crucial steppingstone towards experimental techniques capable of quantifying the two-way interaction between the blast loading and the dynamic response of plated structures. Such techniques will improve the understanding of where blast–structure interaction is of importance (or not) to ensure structural integrity during blast loading events.
- The outcomes of the present study motivate further work on load reconstruction during the dynamic response of plated structures in other extreme loading environments. In particular, the methodology developed in this study is directly applicable to obtain new, unique insight into surface pressure distributions on plated structures subjected to slamming ocean waves and other similar impact events.

Data availability

The data generated in this study is available at [44]. The code required for processing, including phase detection and pressure reconstruction, is published in [42].

Acknowledgments

This work has been carried out with financial support from NTNU and the Research Council of Norway (RCN) through the Centre for Advanced Structural Analysis (CASA), Centre for Research-based Innovation (RCN Project No. 237885); SINTEF Ocean and the SLADE KPN project (RCN Project No. 294748); and the Norwegian Ministry of Justice and Public Security.

Declaration of competing interest

The authors declare that they have no known competing financial interests or personal relationships that could have appeared to influence the work reported in this paper.

References

[1] Tiwari V, Sutton MA, McNeill SR, Xu S, Deng X, Fourney WL, et al. Application of 3D image correlation for full-field transient plate deformation measurements during blast loading. Int J Impact Eng 2009;36:862–74. http://dx.doi.org/10.1016/j.ijimpeng.2008.09.010.

[2] Spranghers K, Vasilakos I, Lecompte D, Sol H, Vantomme J. Full-field deformation measurements of aluminum plates under free air blast loading. Exp Mech 2012;52:1371–84. http://dx.doi.org/10.1007/s11340-012-9593-5.

[3] Aune V, Fagerholt E, Hauge KO, Langseth M, Børvik T. Experimental study on the response of thin aluminium and steel plates subjected to airblast loading. Int J Impact Eng 2016;90:106–21. http://dx.doi.org/10.1016/j.ijimpeng.2015.11.017.

[4] Curry RJ, Langdon GS. Transient response of steel plates subjected to close proximity explosive detonations in air. Int J Impact Eng 2017;102:102–16. http://dx.doi.org/10.1016/j.ijimpeng.2016.12.004.

[5] Hild F, Bouterf A, Roux S. Measurement of kinematic fields via DIC for impact engineering applications. Int J Impact Eng 2019;130:163–71. http://dx.doi.org/10.1016/j.ijimpeng.2019.04.007.

[6] Badulescu C, Grédiac M, Mathias JD. Investigation of the grid method for accurate in-plane strain measurement. Meas Sci Technol 2009;20(9):095102.

[7] Surrel Y, Fournier N, Grédiac M, Paris P-A. Phase-stepped deflectometry applied to shape measurement of bent plates. Exp Mech 1999;39(1):66–70. http://dx.doi.org/10.1007/BF02329303.

[8] Rigby S, Tyas A, Clarke S, Fay S, Reay J, Warren J, et al. Observations from preliminary experiments on spatial and temporal pressure measurements from near-field free air explosions. Int J Protect Struct 2015;6:175–90. http://dx.doi.org/10.1260/2041-4196.6.2.175.

[9] Rigby S, Fay S, Clarke S, Tyas A, Reay J, Warren J, et al. Measuring spatial pressure distribution from explosives buried in dry leighton buzzard sand. Int J Impact Eng 2016;96:89–104. http://dx.doi.org/10.1016/j.ijimpeng.2016.05.004.

[10] Rigby S, Akintaro O, Fuller B, Tyas A, Curry R, Langdon G, et al. Predicting the response of plates subjected to near-field explosions using an energy equivalent impulse. Int J Impact Eng 2019;128:24–36. http://dx.doi.org/10.1016/j.ijimpeng.2019.01.014.

[11] Aune V, Valsamos G, Casadei F, Langseth M, Børvik T. Fluid-structure interaction effects during the dynamic response of clamped thin steel plates exposed to blast loading. Int J Mech Sci 2021;195:106263. http://dx.doi.org/10.1016/j.ijmecsci.2020.106263.

[12] Jaw Y, Chen J-H, Wu P-C. Measurement of pressure distribution from PIV experiments. J Visual 2009;12:27–35.

[13] de Kat R, van Oudheusden BW. Instantaneous planar pressure determination from PIV in turbulent flow. Exp Fluids 2012;52(5):1089–106.

[14] Schneiders JFG, Caridi GCA, Sciacchitano A, Scarano F. Large-scale volumetric pressure from tomographic PTV with HFSB tracers. Exp Fluids 2016;57(11):164.

[15] Higham J, Isacc O, Rigby S. Optical flow tracking velocimetry of near-field explosions. Meas Sci Technol 2022;33. http://dx.doi.org/10.1088/1361-6501/ac4599.

[16] Beverley J. McKeon RHE. In: Tropea C, Yarin A, Foss J, editors. Springer handbook of experimental fluid mechanics. Springer-Verlag Berlin Heidelberg; 2007, p. 188–208.

[17] Clarke SD, Fay SD, Warren JA, Tyas A, Rigby SE, Elgy I. A large scale experimental approach to the measurement of spatially and temporally localised loading from the detonation of shallow-buried explosives. Meas Sci Technol 2014;26(1):015001. http://dx.doi.org/10.1088/0957-0233/26/1/015001.

[18] Langran-Wheeler C, Rigby S, Clarke S, Tyas A, Stephens C, Walker R. Near-field spatial and temporal blast pressure distributions from non-spherical charges: Horizontally-aligned cylinders. Int J Protect Struct 2021. http://dx.doi.org/10.1177/20414196211013443, published online.
[19] Nurick G, Martin J. Deformation of thin plates subjected to impulsive loading—A review: Part I: Theoretical considerations. Int J Impact Eng 1989;8(2):159–70. http://dx.doi.org/10.1016/0734-743X(89)90014-6.
[20] Nurick GN, J. B. Martin JB. Deformation of thin plates subjected to impulsive loading - A review - part II - experimental results. Int J Impact Eng 1989;8(2):171–86. http://dx.doi.org/10.1016/0734-743X(89)90015-8.
[21] Micallef K, Fallah A, Pope D, Moatamedi M, Louca L. On dimensionless loading parameters for close-in blasts. Int J Multiphys 2015;9(2):171–94. http://dx.doi.org/10.1260/1750-9548.9.2.171.
[22] Chung Kim Yuen S, Nurick G, Langdon G, Iyer Y. Deformation of thin plates subjected to impulsive load: Part III – an update 25 years on. Int J Impact Eng 2017;107:108–17. http://dx.doi.org/10.1016/j.ijimpeng.2016.06.010.
[23] Pezerat C, Guyader J-L. Force analysis technique: Reconstruction of force distribution on plates. Acta Acust United Acust 2000;86(2):322–32.
[24] Lecoq D, Pézerat C, Thomas J-H, Bi W. Extraction of the acoustic component of a turbulent flow exciting a plate by inverting the vibration problem. J Sound Vib 2014;333(12):2505–19. http://dx.doi.org/10.1016/j.jsv.2014.02.003.
[25] Berry A, Robin O, Pierron F. Identification of dynamic loading on a bending plate using the Virtual Fields Method. J Sound Vib 2014;333(26):7151–64. http://dx.doi.org/10.1016/j.jsv.2014.08.038.
[26] Berry A, Robin O. Identification of spatially correlated excitations on a bending plate using the Virtual Fields Method. J Sound Vib 2016;375:76–91. http://dx.doi.org/10.1016/j.jsv.2016.03.042.
[27] Robin O, Berry A. Estimating the sound transmission loss of a single partition using vibration measurements. Appl Acoust 2018;141:301–6. http://dx.doi.org/10.1016/j.apacoust.2018.07.015.
[28] O'Donoughue P, Robin O, Berry A. Time-resolved identification of mechanical loadings on plates using the virtual fields method and deflectometry measurements. Strain 2017;54(3):e12258. http://dx.doi.org/10.1111/str.12258.
[29] Kaufmann R, Pierron F, Ganapathisubramani B. Full-field surface pressure reconstruction using the Virtual Fields Method. Exp Mech 2019;59(8):1203–21. http://dx.doi.org/10.1007/s11340-019-00530-2.
[30] Kaufmann R, Pierron F, Ganapathisubramani B. Reconstruction of surface pressure fluctuations using deflectometry and the virtual fields method. Exp Fluids 2020;61(35). http://dx.doi.org/10.1007/s00348-019-2850-y.
[31] Kaufmann R, Ganapathisubramani B, Pierron F. Surface pressure reconstruction from phase averaged deflectometry measurements using the virtual fields method. Exp Mech 2020;60:379–92. http://dx.doi.org/10.1007/s11340-019-00530-2.
[32] Pierron F, Grédiac M. the virtual fields method. extracting constitutive mechanical parameters from full-field deformation measurements. Springer New-York; 2012, p. 517.
[33] Toussaint E, Grédiac M, Pierron F. The virtual fields method with piecewise virtual fields. Int J Mech Sci 2006;48(3):256–64. http://dx.doi.org/10.1016/j.ijmecsci.2005.10.002.
[34] Aune V, Fagerholt E, Langseth M, Børvik T. A shock tube facility to generate blast loading on structures. Int J Protect Struct 2016;7(3):340–66. http://dx.doi.org/10.1177/2041419616666236.
[35] Raffel M. Background-oriented schlieren (BOS) techniques. Exp Fluids 2015;56(3):60. http://dx.doi.org/10.1007/s00348-015-1927-5.
[36] Surrel Y. Design of algorithms for phase measurements by the use of phase stepping. Appl Opt 1996;35(1):51–60. http://dx.doi.org/10.1364/AO.35.000051.
[37] Poon CY, Kujawinska M, Ruiz C. Spatial-carrier phase shifting method of fringe analysis for moiré interferometry. J Strain Anal Eng Des 1993;28(2):79–88. http://dx.doi.org/10.1243/03093247V282079.
[38] Surrel Y. Photomechanics. Berlin, Heidelberg: Springer Berlin Heidelberg; 2000, p. 55–102. http://dx.doi.org/10.1007/3-540-48800-6_3.
[39] Ritter R. Reflection moire methods for plate bending studies. Opt Eng 1982;21:21–9. http://dx.doi.org/10.1117/12.7972962.
[40] Zienkiewicz O. The finite element method. McGraw-Hill; 1977.
[41] D'Errico J. Inverse (integrated) gradient. 2009, URL: h (Accessed June 12 2019).
[42] Olufsen S, Kaufmann R, Fagerholt E, Aune V. RECOLO: A python package for the reconstruction of surface pressure loads from kinematic fields using the virtual fields method. Journal of Open Source Software 2021;6(67):3869. http://dx.doi.org/10.21105/joss.03869.
[43] Rossi M, Pierron F. On the use of simulated experiments in designing tests for material characterization from full-field measurements. Int J Solids Struct 2012;49(3):420–35. http://dx.doi.org/10.1016/j.ijsolstr.2011.09.025.
[44] Kaufmann R, Aune V. Experimental data for 'Reconstruction of Surface Pressures on Flat Plates Impacted by Blast Waves Using the Virtual Fields Method'. DataverseNO 2022. http://dx.doi.org/10.18710/GXKVUR.